

Tuning the Magnetic Ordering Temperature of Hexagonal Ferrites by Structural Distortion Control

Kishan Sinha¹, Haohan Wang¹, Xiao Wang², Liying Zhou^{3,4}, Yuewei Yin¹, Wenbin Wang⁵, Xuemei Cheng², David J Keavney⁶, Huibo Cao⁷, Yaohua Liu⁷, Xifan Wu³, Xiaoshan Xu^{1,8}

¹*Department of Physics and Astronomy, University of Nebraska, Lincoln, Nebraska 68588, USA,*

²*Department of Physics, Bryn Mawr College, Bryn Mawr, Pennsylvania 19010, USA*

³*Department of Physics, Temple University, Philadelphia, Pennsylvania 19122, USA*

⁴*International Center for Quantum Materials and School of Physics, Peking University, Beijing 100871, People's Republic of China*

⁵*Department of Physics, Fudan University, Shanghai 200433, People's Republic of China*

⁶*Advanced Photon Source, Argonne National Laboratory, Argonne, Illinois 60439, USA*

⁷*Neutron Scattering Division, Oak Ridge National Laboratory, Oak Ridge, TN 37831, USA*

⁸*Nebraska Center for Materials and Nanoscience, University of Nebraska, Lincoln, Nebraska 68588, USA*

Abstract

To tune the magnetic properties of hexagonal ferrites, a family of magnetoelectric multiferroic materials, by atomic-scale structural engineering, we studied the effect of structural distortion on the magnetic ordering temperature (T_N). Using the symmetry analysis, we show that unlike most antiferromagnetic rare-earth transition-metal perovskites, a larger structural distortion leads to a higher T_N in hexagonal ferrites and manganites, because the K_3 structural distortion induces the three-dimensional magnetic ordering, which is forbidden in the undistorted structure by symmetry. We also revealed a near-linear relation between T_N and the tolerance factor and a power-law relation between T_N and the K_3 distortion amplitude. Following the analysis, a record-high T_N (185 K) among hexagonal ferrites was predicted in hexagonal ScFeO_3 and experimentally verified in epitaxially stabilized films. These results add to the paradigm of spin-lattice coupling in antiferromagnetic oxides and suggests further tunability of hexagonal ferrites if more lattice distortion can be achieved.

Spin-lattice couplings have a significant impact on magnetic properties. In antiferromagnetic (AFM) orthorhombic $RTMO_3$ (o - $RTMO_3$) for example, where R stands for rare earth, Y, or Sc, and TM stands for transition metal, a larger orthorhombic distortion from the cubic perovskite structure correlates with a lower Neel temperature (T_N) [see supplementary information], which may be understood as the reduction of the AFM super-exchange interactions caused by the smaller TM -O- TM bond angles due to the orthorhombic distortions [1,2].

The effect of spin-lattice couplings may be employed to tune the magnetic properties. Here we focus on increasing the T_N of hexagonal $RFeO_3$ (h - $RFeO_3$), a family of multiferroics materials that are promising candidates for applications because of their spontaneous electric and magnetic polarizations, and potential magnetoelectric effects due to the coupling between the ferroelectric and the magnetic orders [3,4]. For widespread applications, it is important to increase the T_N of h - $RFeO_3$ [5], by, e.g. atomic-scale structural engineering based on the spin-lattice couplings.

On the other hand, in h - $RFeO_3$, T_N increases with the lattice distortion, which is a puzzling trend opposite to that in the AFM o - $RTMO_3$ [see supplementary information]. Previously, Disseler et al. discovered a correlation between T_N and lattice constants in h - $RMnO_3$ and h - $RFeO_3$ [6]. The higher T_N for smaller R has been attributed to closer Fe-Fe (or Mn-Mn) distances [6,7]. This understanding is worth revisiting, since it cannot explain that in AFM o - $RTMO_3$, the smaller lattice constants do bring the TM atoms closer, but the reduced TM -O- TM bond angles actually decreases the AFM exchange interactions and T_N . Hence, there should be a distinct mechanism of magnetic ordering and spin-lattice coupling in h - $RFeO_3$. Elucidating this mechanism will not only provide guidance in increasing T_N of h - $RFeO_3$, but also add to the paradigms of spin-lattice coupling in AFM materials.

In this work, we examine the role of the structural distortion in the magnetic ordering in h - $RMnO_3$ and h - $RFeO_3$. A symmetry analysis shows that the three-dimensional magnetic ordering is forbidden in the undistorted structure by symmetry, but can be induced by the K_3 distortion with a power-law relation between T_N and K_3 magnitude. Based on these revelations, we have predicted a record-high T_N in h - $RFeO_3$ when R =Sc and experimentally confirmed it in epitaxially stabilized films.

Hexagonal $ScFeO_3$ (001) and $YbFeO_3$ (001) films (5×5 mm² and 10×10 mm² surface area, 70-200 nm thick) have been grown on Al_2O_3 (001) and yttrium stabilized zirconia (YSZ) (111) respectively using pulsed laser (248 nm) deposition in a 5 mTorr oxygen environment, at 750 °C with a laser fluence of about 1.5 J/cm² and a repetition rate of 2 Hz [8]. The film growth was monitored using the reflection high-energy electron diffraction (RHEED). The structural and magnetic properties have been studied using x-ray diffraction and spectroscopy, magnetometry and neutron diffraction. X-ray diffraction experiments, including $\theta/2\theta$ scan, φ scan, and reciprocal space mapping were carried out using a Rigaku D/Max-B diffractometer with Co-K α radiation (1.793 Å wave length) and a Rigaku SmartLab diffractometer with Cu-K α radiation (1.5406 Å). X-ray absorption spectroscopy (including x-ray linear dichroism) with a 20° incident angle was studied at beamline 4-ID-C at the Advanced Photon Source at Argonne National Laboratory. Neutron diffraction experiments were carried out at beamline CORELLI at the Spallation Neutron Source (SNS) and HB3A four-circle diffractometer (FCD) at the High Flux Reactor (HFIR) with a thermal neutron wavelength of 1.546 Å, in the Oak Ridge National Laboratory. Temperature and magnetic-field dependence of the magnetization was measured using a superconducting quantum interference device (SQUID) magnetometer with the field along the film normal direction.

The crystal structure of isomorphous hexagonal $RMnO_3$ and $RFeO_3$ (h - $RMnO_3$ and h - $RFeO_3$) has a $P6_3cm$ symmetry, consisting of alternating FeO (or MnO) and RO_2 layers [Fig. 1(a)]. AFM orders occur in h - $RMnO_3$ and h - $RFeO_3$ below about 70-140 K with spins in the FeO (or MnO) layers forming 120-degree

structures [6,9–12]. Below about 1000 K, ferroelectricity in h-RMnO₃ and h-RFeO₃ is induced by a lattice distortion (K₃) [Fig. 1(a)] that tilts the FeO₅ (or MnO₅) local environment, shifts the *R* atoms along the *c* axis, and trimerizes the unit cell, with a sizable electric polarization ($P \sim 10 \mu\text{C}/\text{cm}^2$) [13–16]. In addition, hexagonal RFeO₃ exhibits a weak ferromagnetism [10,12,14,15,17,18] [Fig. 1(a)] due to the canting Fe spins.

Magnetic ordering relies on the underlying exchange interactions. In h-RFeO₃ and h-RMnO₃, although the exchange interactions within the FeO (or MnO) layers are strong, the inter-layer exchange interactions are weakened by the topology of layered structure and hexagonal stacking. Using h-RFeO₃ as an example, Fig. 1(b) shows the arrangement of the Fe atoms and their spins in two neighboring FeO layers. The Fe atoms are on the hexagonal A and C sites in the two layers respectively. One Fe atom (Fe₀) in the $z = c/2$ layer is highlighted by its tilted FeO₅ trigonal bipyramid. The interlayer nearest-neighbor exchange energy for Fe₀ is $E_{inter} = \sum_{i=1}^3 J_{0i} \vec{S}_0 \cdot \vec{S}_i$, where \vec{S}_i is the spin on Fe_{*i*}, and J_{0i} is the exchange interaction coefficient between Fe₀ and Fe_{*i*}. When there is no lattice distortion, the local symmetry of Fe₀ is C_{3v}, leading to $J_{01}=J_{02}=J_{03}$ and $E_{inter}=0$ because $\sum_{i=1}^3 \vec{S}_i = 0$. In other words, the interlayer exchange are canceled; the spin alignment between the two layers is lost. Therefore, the three-dimensional magnetic ordering is forbidden in the undistorted P6₃/mmc structure by symmetry.

On the other hand, the K₃ lattice distortion [Fig. 1(a)] reduces the symmetry to C_s, making $J_{01}=J_{02} \neq J_{03}$. Consequently, nonzero lattice distortion leads to the three-dimensional magnetic ordering because $E_{inter}=(J_{01}-J_{03})S(S+1) \neq 0$ [19]. Since the inter-layer exchange interaction is the bottleneck of the three-dimensional magnetic ordering, one has $T_N \propto E_{inter} = (J_{01}-J_{03})S(S+1)$. The dependence of T_N on the K₃ distortion then hinges on the relation between $J_{01}-J_{03}$ and the magnitude of K₃ (Q_{K3}). Previously, Das et al. analyzed the relation between $J_{01}-J_{03}$ and Q_{K3} [3]. Expanding J_{01} and J_{03} with respect to Q_{K3} around $Q_{K3}=0$, the odd terms are expected to be zero due to the symmetry at $Q_{K3}=0$, leaving $J_{01}-J_{03} \propto a_2 Q_{K3}^2 + a_4 Q_{K3}^4$, where a_2 and a_4 are coefficients. In Fig. 1(c), we plot the $\log\{T_N/[S(S+1)]\}$ as a function of $\log(Q_{K3})$ of h-RMnO₃ measured using the neutron diffraction from the literature [20,21] [see supplementary information], where spin S is 2 for Mn. The data appear to fall on a straight line, indicating a power-law relation $T_N/[S(S+1)] \propto Q_{K3}^n$; a fit shows $n = 2.7 \pm 0.05$. Given that the tilt of FeO₅ and MnO₅ caused by the K₃ distortion is on the order of 5 degrees [9,20,21] which is not so small, both the $a_2 Q_{K3}^2$ and the $a_4 Q_{K3}^4$ terms could play a role, resulting $2 < n < 4$.

It is challenging to predict the T_N using the direct dependence of T_N on the K₃ distortion though, because the K₃ distortion, which involves the displacement of oxygen atoms, is difficult to measure precisely. Tolerance factor $t=(r_R+r_O)/(r_{TM}+r_O)\sqrt{2}$ where r_R , r_{TM} , and r_O are atomic radius of *R*, *TM* and oxygen, is a good measure of lattice distortion from the cubic perovskite structure in o-RTMO₃. It could also be used to gauge the structural distortion in h-RFeO₃ and h-RMnO₃, because a smaller *R* atom is expected to reduce the in-plane lattice constant, which needs to be accommodated by a larger K₃ distortion to reduce the distances between Fe (or Mn) atoms within the FeO (or MnO) layers. In other words, smaller t is expected to lead to larger T_N , which is consistent with the data from the literature [Fig. 1(c) inset] [11,20,21], where a linear correlation between $T_N/[S(S+1)]$ and t in h-RFeO₃ and h-RMnO₃ is observed ($S = 2$ and 2.5 for Mn and Fe respectively).

Following the trend in Fig. 1(c), a smaller *R*, corresponding to a smaller t , will lead to a higher T_N in h-RFeO₃ and h-RMnO₃. Since Sc has much smaller atomic radius than the rare earth and Y [22], T_N in h-ScFeO₃ is expected to be higher than that of other h-RFeO₃. To verify the prediction, we studied the magnetic ordering temperature in h-ScFeO₃. ScFeO₃ naturally crystallizes in bixbyite structure in bulk; high pressure growth of ScFeO₃ results in a corundum structure [23]. Previous studies show that partially

substituting Lu with Sc in LuFeO_3 may stabilize the hexagonal structure [6,7,24]. However, the stabilization of pure ScFeO_3 in the $\text{P6}_3\text{cm}$ structure has never been reported. In this study, we have successfully grown h-ScFeO_3 epitaxial films on Al_2O_3 (001) substrates. The crystal structure and epitaxial relations of the h-ScFeO_3 films were characterized using x-ray diffraction. As shown in Fig. 2(a), the $\theta/2\theta$ scan shows a typical pattern of the $\text{P6}_3\text{cm}$ structure with the epitaxial relation: h-ScFeO_3 (001) \parallel Al_2O_3 (001). The φ scan [see supplementary information] demonstrates the six-fold rotation symmetry and the in-plane epitaxial relation: h-ScFeO_3 (100) \parallel Al_2O_3 (100). The RHEED patterns [Fig. 2(b) and (c)], which are signatures of the h-RFeO_3 structure, indicate a flat surface. The FeO_5 trigonal bipyramid configuration is confirmed by the similarity between the x-ray linear dichroism spectroscopy of h-ScFeO_3 [Fig. 2(d)] and those of h-LuFeO_3 and h-YbFeO_3 observed previously [8,25–27]. From the x-ray reciprocal space mapping [see supplementary information], the lattice constants of h-ScFeO_3 were determined: $a = 5.742 \text{ \AA}$ and $c = 11.690 \text{ \AA}$, smaller than the values of other h-RFeO_3 [28–30], suggesting a larger lattice distortion [31].

T_N of h-ScFeO_3 was measured by the neutron diffraction experiments at CORELLI in addition to that of h-YbFeO_3 . Using a wide wavelength-band neutron beam and a two-dimensional detector at CORELLI, a three-dimensional portion of the reciprocal space [using the Miller indices (H, K, L) as the coordinates] can be measured without rotating the sample [See supplementary materials]. The (101) and (114) diffraction peaks, were mapped out in the three-dimensional reciprocal space. As shown in Fig. 2(e), the two magnetic Bragg diffraction peaks (101) and (1-11), which are equivalent because of the six-fold rotational symmetry along the c axis, were observed. The (101) Bragg peak is forbidden for the nuclear diffraction due to the crystal structure symmetry of h-RFeO_3 (space group $\text{P6}_3\text{cm}$), but it is allowed for magnetic diffraction [9]. The observation of the (101) peak confirms the magnetic ordering in h-RFeO_3 , as previously shown in h-LuFeO_3 and h-RMnO_3 [6,9,12]. The temperature dependence of the (101) peak intensity suggests a transition at about 200 K, which is corroborated by the measurements at HB3A [Fig. 2(f)]. In contrast, the intensity of the (114) peak, which mainly comes from the nuclear scattering, shows an insignificant temperature dependence. As shown in Fig. 2(g), a similar transition temperature is observed in the temperature dependence of the magnetization measured using a SQUID magnetometer on warming, after cooling the sample in a 10 kOe magnetic field (field cool or FC) and after cooling in a zero magnetic field (zero-field cool or ZFC). The FC and ZFC curves diverge at around 185 K, giving a more precise determination of T_N .

As predicted, h-ScFeO_3 shows a high T_N among all h-RMnO_3 and h-RFeO_3 , as shown in Fig. 3(a), where our measurement on h-YbFeO_3 and data in the literature are also included [See supplementary information] [6,9,11–15,17,21]; the measured T_N of h-ScFeO_3 is slightly lower than the value predicted by extrapolating the linear relation between T_N and t , which is also true for h-ScMnO_3 [9]. The reduction of magnetization at low temperature in Fig. 2(g) hints a possible spin reorientation at about 100 K in h-ScFeO_3 . However, the temperature dependence of the (101) peak intensity in Fig. 2(f) indicates that spin reorientation in h-ScFeO_3 may not be significant enough to change the spin structure from A_2 to A_1 [6].

Finally, we discuss the effect of lattice distortion on the canting of Fe moments, which is responsible for the net magnetization M_{Fe} along the c axis. The M_{Fe} in h-ScFeO_3 can be inferred from the magnetometry data. As shown in Fig. 2(h), the M - H curve shows a soft and a hard component, corresponding to two steps at $H \approx 0$ and $H \approx 30$ kOe respectively. This two-component feature has been observed in both h-LuFeO_3 and h-YbFeO_3 films [18,25]. The jump of magnetization at the higher field corresponds to the intrinsic coercivity of the h-RFeO_3 , while the jump at low field corresponds to the unavoidable structural boundaries in film samples of h-RFeO_3 that create uncompensated spins. From the 30-kOe jump, we found that $M_{\text{Fe}} = 0.015 \pm 0.002 \mu_B/\text{Fe}$ in h-ScFeO_3 , which is smaller than that of h-LuFeO_3 and h-YbFeO_3 [18,25], as shown in Fig. 3(b). This result is counter-intuitive, because a large K_3 distortion, corresponding to a larger tilt

angle of the FeO₅ would seemingly generate a larger canting angle of the Fe moments (θ_{cant}). However, θ_{cant} results from a competition between the exchange interaction and the Dzyaloshinskii-Moriya (DM) interaction [32–34]. Relation between the canting angle (θ_{cant}) of the Fe moments, tilt angle of the FeO₅ (γ_{tilt}), lattice constant in the basal plane (a), and the intralayer exchange interaction coefficient J can be derived as $\theta_{\text{cant}} \propto a^2 \gamma_{\text{tilt}} / J$ [See supplementary materials]. Although h-ScFeO₃ is expected to have a larger γ_{tilt} and smaller J , a is also smaller. Hence, the size of θ_{cant} cannot be simply linked to the amplitude of γ_{tilt} . If the effect of a dominates, M_{Fe} would decrease for smaller R , which is what we found in our previous first-principle calculations [31].

In conclusion, using symmetry analysis, we showed that the three-dimensional magnetic ordering in h-RMnO₃ and h-RFeO₃ are forbidden in undistorted structures by symmetry, but can be induced by the structural distortions. We also showed that dependence of T_{N} on structural distortions manifests as a near-linear relation with the tolerance factor and a possible power law with $Q_{\text{K}3}$, suggesting a higher T_{N} in h-ScFeO₃ with respect to other hexagonal ferrites studied so far, which was realized in this work in epitaxially stabilized films. In addition to indicating that the multiferroic ordering in h-RFeO₃ and h-RMnO₃ may be further enhanced with larger lattice distortions, these results also establish a paradigm of structural origin of magnetic ordering and spin-lattice coupling in AFM oxides.

Acknowledgement

This work was primarily supported by the National Science Foundation (NSF), Division of Materials Research (DMR) under Award No. DMR-1454618. X.W. was supported by National Science Foundation through Award No. DMR-1552287. X.M.C. acknowledges partial support from NSF DMR-1708790 and DMR-1053854. This research used resources at the Spallation Neutron Source and the High Flux Isotope Reactor, DOE Office of Science User Facilities operated by the Oak Ridge National Laboratory, and resources of the Advanced Photon Source, a U.S. Department of Energy (DOE) Office of Science User Facility operated for the DOE Office of Science by Argonne National Laboratory under Contract No. DE-AC02-06CH11357. The research was performed in part in the Nebraska Nanoscale Facility: National Nanotechnology Coordinated Infrastructure and the Nebraska Center for Materials and Nanoscience, which are supported by the National Science foundation under award ECCS: 1542182, and the Nebraska Research Initiative.

References

- [1] J. B. Goodenough, *J. Phys. Chem. Solids* **6**, 287 (1958).
- [2] J. Kanamori, *J. Phys. Chem. Solids* **10**, 87 (1959).
- [3] H. Das, A. L. Wysocki, Y. Geng, W. Wu, and C. J. Fennie, *Nat. Commun.* **5**, 2998 (2014).
- [4] M. Ye and D. Vanderbilt, *Phys. Rev. B* **92**, 035107 (2015).
- [5] J. A. Mundy, C. M. Brooks, M. E. Holtz, J. A. Moyer, H. Das, A. F. Rébola, J. T. Heron, J. D. Clarkson, S. M. Disseler, Z. Liu, A. Farhan, R. Held, R. Hovden, E. Padgett, Q. Mao, H. Paik, R. Misra, L. F. Kourkoutis, E. Arenholz, A. Scholl, J. A. Borchers, W. D. Ratcliff, R. Ramesh, C. J. Fennie, P. Schiffer, D. A. Muller, and D. G. Schlom, *Nature* **537**, 523 (2016).
- [6] S. M. Disseler, X. Luo, B. Gao, Y. S. Oh, R. Hu, Y. Wang, D. Quintana, A. Zhang, Q. Huang, J. Lau, R. Paul, J. W. Lynn, S. W. Cheong, and W. Ratcliff, *Phys. Rev. B* **92**, 054435 (2015).
- [7] A. Masuno, A. Ishimoto, C. Moriyoshi, N. Hayashi, H. Kawaji, Y. Kuroiwa, and H. Inoue, *Inorg. Chem.* **52**, 11889 (2013).
- [8] S. Cao, X. Zhang, T. R. Paudel, K. Sinha, X. Wang, X. Jiang, W. Wang, S. Brutsche, J. Wang, P. J. Ryan, J.-W. Kim, X. Cheng, E. Y. Tsymbal, P. A. Dowben, and X. Xu, *J. Phys. Condens. Matter* **28**, 156001 (2016).
- [9] A. Munoz, J. A. Alonso, M. J. Martinez-Lope, M. T. Casais, J. L. Martinez, and M. T. Fernandez-Diaz, *Phys. Rev. B* **62**, 9498 (2000).
- [10] W. Wang, J. Zhao, W. W. Wang, Z. Gai, N. Balke, M. Chi, H. N. H. N. Lee, W. Tian, L. Zhu, X. Cheng, D. J. D. J. Keavney, J. Yi, T. Z. T. Z. Ward, P. C. P. C. P. C. Snijders, H. M. H. M. Christen, W. Wu, J. Shen, and X. Xu, *Phys. Rev. Lett.* **110**, 237601 (2013).
- [11] M. Fiebig, T. Lottermoser, and R. V. Pisarev, *J. Appl. Phys.* **93**, 8194 (2003).
- [12] S. M. Disseler, J. A. Borchers, C. M. Brooks, J. A. Mundy, J. A. Moyer, D. A. Hillsberry, E. L. Thies, D. A. Tenne, J. Heron, M. E. Holtz, J. D. Clarkson, G. M. Stiehl, P. Schiffer, D. A. Muller, D. G. Schlom, and W. D. Ratcliff, *Phys. Rev. Lett.* **114**, 217602 (2015).
- [13] Y. K. Jeong, J. H. Lee, S. J. Ahn, and H. M. Jang, *Chem. Mater.* **24**, 2426 (2012).
- [14] Y. K. Jeong, J. Lee, S. Ahn, S.-W. Song, H. M. Jang, H. Choi, and J. F. Scott, *J. Am. Chem. Soc.* **134**, 1450 (2012).
- [15] S.-J. Ahn, J.-H. Lee, H. M. Jang, and Y. K. Jeong, *J. Mater. Chem. C* **2**, 4521 (2014).
- [16] P. Murugavel, J. H. Lee, D. Lee, T. W. Noh, Y. Jo, M. H. Jung, Y. S. Oh, and K. H. Kim, *Appl. Phys. Lett.* **90**, 142902 (2007).
- [17] H. Yokota, T. Nozue, S. Nakamura, H. Hojo, M. Fukunaga, P. E. Janolin, J. M. Kiat, and A. Fuwa, *Phys. Rev. B* **92**, 054101 (2015).
- [18] J. A. Moyer, R. Misra, J. A. Mundy, C. M. Brooks, J. T. Heron, D. A. Muller, D. G. Schlom, and P. Schiffer, *APL Mater.* **2**, 012106 (2014).
- [19] H. Wang, I. V. Solovyev, W. Wang, X. Wang, P. J. Ryan, D. J. Keavney, J.-W. Kim, T. Z. Ward, L. Zhu, J. Shen, X. M. Cheng, L. He, X. Xu, and X. Wu, *Phys. Rev. B* **90**, 014436 (2014).
- [20] S. Lee, A. Pirogov, M. Kang, K.-H. H. Jang, M. Yonemura, T. Kamiyama, S.-W. S.-W. W.

- Cheong, F. Gozzo, N. Shin, H. Kimura, Y. Noda, and J.-G. G. J.-G. Park, *Nature* **451**, 805 (2008).
- [21] A. Munoz, J. Alonso, M. Martinez-Lopez, M. Cesais, J. Martinez, and M. Fernandez-Diaz, *Chem. Mater.* **13**, 1497 (2001).
- [22] R. D. Shannon, *Acta Cryst.* **A32**, 751 (1976).
- [23] M. Li, U. Adem, S. R. C. Mcmitchell, Z. Xu, C. I. Thomas, J. E. Warren, D. V Giap, H. Niu, X. Wan, R. G. Palgrave, F. Schiffmann, F. Cora, B. Slater, T. L. Burnett, M. G. Cain, A. M. Abakumov, G. Van Tendeloo, M. F. Thomas, M. J. Rosseinsky, and J. B. Claridge, *J. Am. Chem. Soc.* **134**, 3737 (2012).
- [24] L. Lin, H. M. Zhang, M. F. Liu, S. Shen, S. Zhou, D. Li, X. Wang, Z. B. Yan, Z. D. Zhang, J. Zhao, S. Dong, and J.-M. Liu, *Phys. Rev. B* **93**, 075146 (2016).
- [25] S. Cao, K. Sinha, X. X. Zhang, X. X. Zhang, X. Wang, Y. Yin, A. T. A. T. N'Diaye, J. Wang, D. J. D. J. Keavney, T. R. T. R. Paudel, Y. Liu, X. Cheng, E. Y. E. Y. Tsymbal, P. A. P. A. Dowben, and X. Xu, *Phys. Rev. B* **95**, 224428 (2017).
- [26] W. Wang, H. Wang, X. Xu, L. Zhu, L. He, E. Wills, X. Cheng, D. J. Keavney, J. Shen, X. Wu, and X. Xu, *Appl. Phys. Lett.* **101**, 241907 (2012).
- [27] S. Cao, X. Zhang, K. Sinha, W. Wang, J. Wang, P. A. Dowben, and X. Xu, *Appl. Phys. Lett.* **108**, 202903 (2016).
- [28] X. Zhang, Y. Yin, S. Yang, Z. Yang, and X. Xu, *J. Phys. Condens. Matter* **29**, 164001 (2017).
- [29] E. Magome, C. Moriyoshi, Y. Kuroiwa, A. Masuno, and H. Inoue, *Jpn. J. Appl. Phys.* **49**, 09ME06 (2010).
- [30] A. A. Bossak, I. E. Graboy, O. Y. Gorbenko, A. R. Kaul, M. S. Kartavtseva, V. L. Svetchnikov, and H. W. Zandbergen, *Chem. Mater.* **16**, 1751 (2004).
- [31] K. Sinha, Y. Zhang, X. Jiang, H. Wang, X. Wang, X. Zhang, P. J. Ryan, J.-W. Kim, J. Bowlan, D. A. Yarotski, Y. Li, A. D. DiChiara, X. Cheng, X. Wu, and X. Xu, *Phys. Rev. B* **95**, 094110 (2017).
- [32] I. Dzyaloshinsky, *J. Phys. Chem. Solids* **4**, 241 (1958).
- [33] T. Moriya, *Phys. Rev.* **120**, 91 (1960).
- [34] F. Keffer, *Phys. Rev.* **126**, 896 (1962).

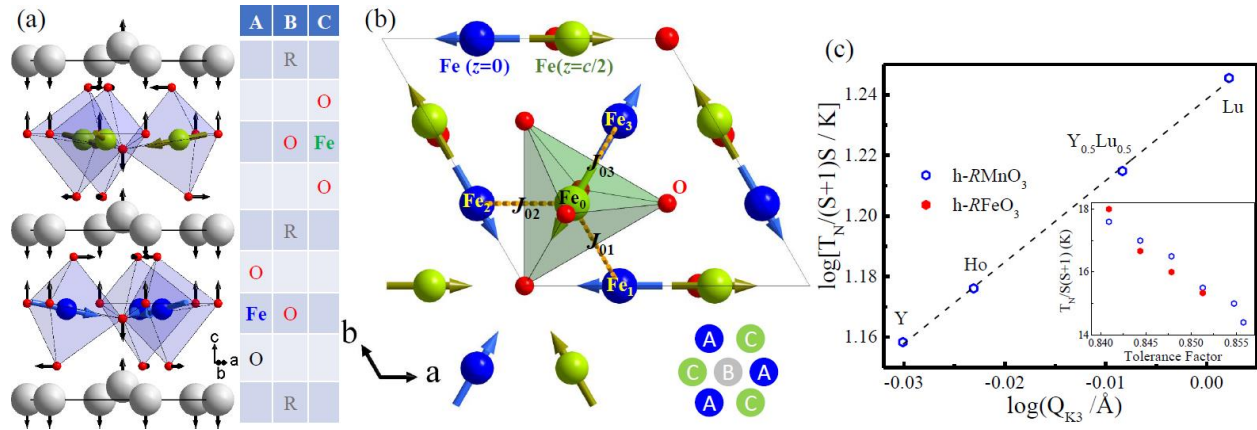


Figure 1. (a) Atomic structure of h-RFeO₃ depicted by a hexagonal unit cell. The arrows through the Fe atoms indicate the spins. The arrows from the atoms indicate the atomic displacements of the K₃ lattice distortion. The table indicates the hexagonal stacking. (b) The geometric arrangement of Fe atoms in the $z=0$ and $z=c/2$ layers. The arrows through the Fe atoms indicate the spin directions. The atom Fe₀ is highlighted by its FeO₅ trigonal bipyramid to depict the local symmetry. (c) $\log\{T_N/[S(S+1)]\}$ as a function of $\log(Q_{K3})$. Inset: $T_N/[S(S+1)]$ as a function of the tolerance factor. The dashed line is a linear fit to the data. The data are from the literature (see text).

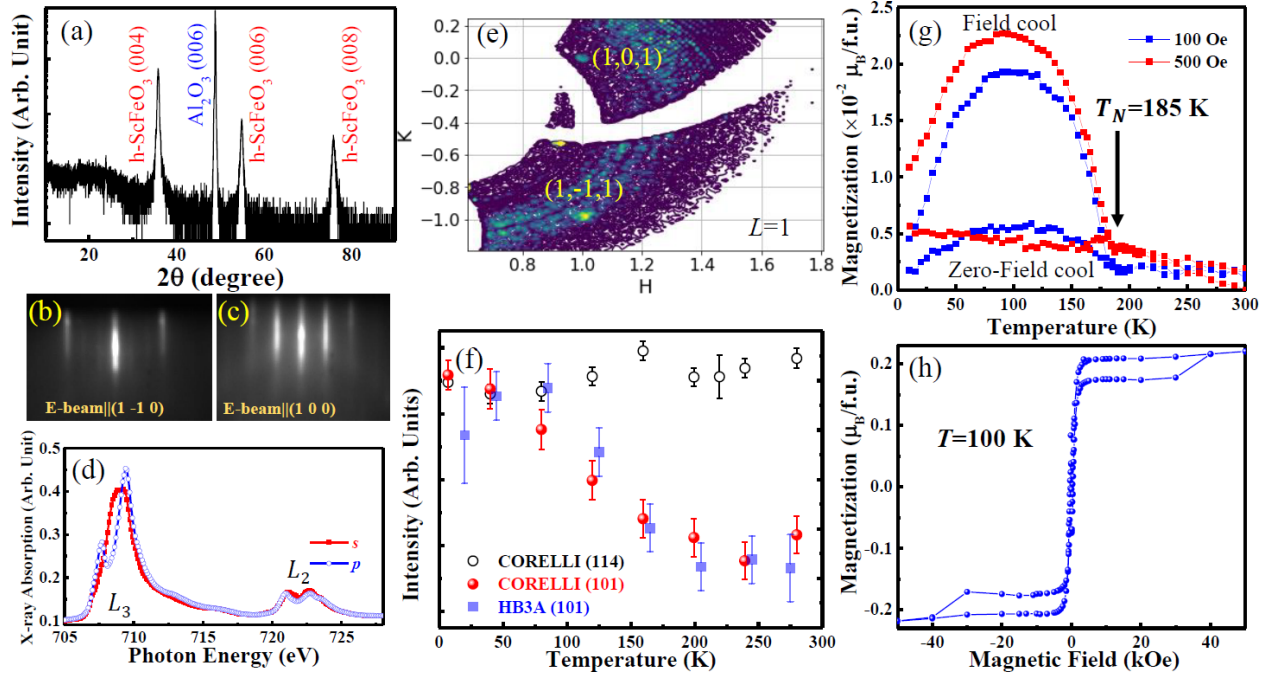


Figure 2. Structural and magnetic characterizations of h-ScFeO₃(001)/Al₂O₃ films. (a) $\theta/2\theta$ x-ray diffraction measured using an x-ray wavelength 1.789 Å. (b) and (c) are the RHEED diffraction patterns measured when the electron beam are along the (1-10) and (100) directions. (d) X-ray absorption spectra measured at the Fe L edges using s (in plane) and p (out of plane) linearly polarized x-ray beams. (e) A slice of the reciprocal space of h-ScFeO₃ at $L=1$ measured using neutron diffraction at CORELLI. (f) Temperature dependence of the neutron diffraction intensities of the (101) and (114) peaks measured at CORELLI and HB3A. (g) Temperature dependence of the magnetization per formula unit (f.u.) measured during warming after field-cool (10 kOe) and zero-field-cool using 100 Oe and 500 Oe. (h) Magnetization-field hysteresis loop measured at 100 K. The field is along the film normal direction.

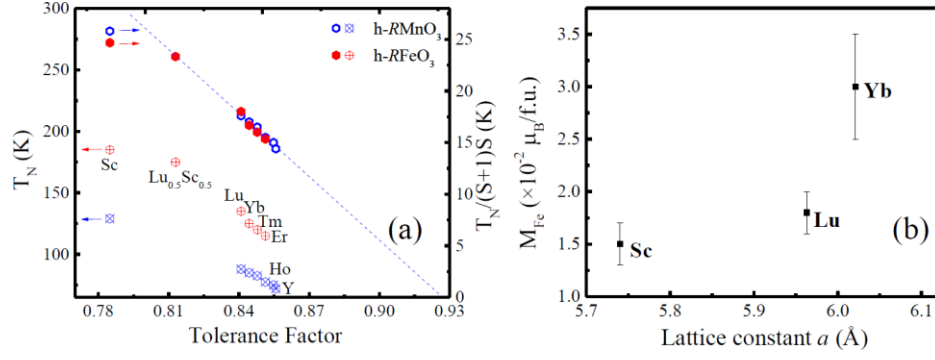


Figure 3. (a) The dependence of T_N and $T_N/S(S+1)$ on the tolerance factor. The dashed line is a guide to the eye. (b) The magnetization from the canting of Fe spins (M_{Fe}) as a function of the in-plane lattice constant. Except for h-YbFeO₃ and h-ScFeO₃ in (a) and h-ScFeO₃ in (b), the data are from the literature (see text).

Supplementary material

S1. Neel temperatures of antiferromagnetic $RTMO_3$

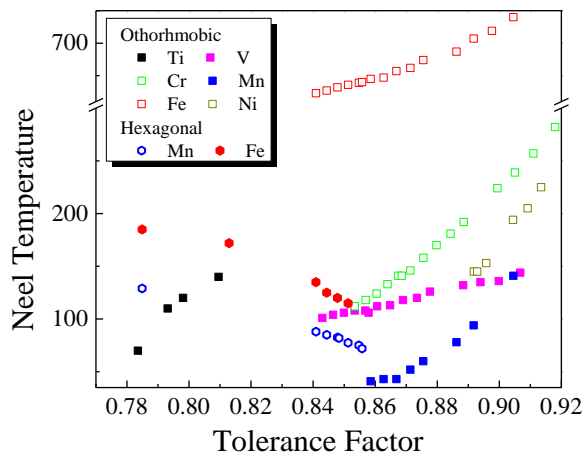


Figure S1. The Neel temperature of orthorhombic antiferromagnetic $RTMO_3$.

In Fig. S1, we surveyed the Neel temperature of antiferromagnetic $RTMO_3$ with orthorhombic and hexagonal structures, where R stands for rare earth, Y, or Sc, TM stands for transition metal. The results are plotted as a function of the tolerance factor [1,2], defined as $t=(r_R+r_O)/(r_{TM}+r_O)\sqrt{2}$, where r_R , r_{TM} , and r_O are atomic radius of R , TM and oxygen. For orthorhombic $RTMO_3$ (o- $RTMO_3$), when t decreases from 1, corresponding to orthorhombic distortions from the cubic perovskite structure, T_N decreases. In contrast, for hexagonal $RTMO_3$ (h- $RTMO_3$), when t decreases, T_N increases.

$RTiO_3$ crystalize in orthorhombic structure. When the size of R is smaller than that of Sm, the materials become ferromagnetic [3].

RVO_3 and $RCrO_3$ both crystalize in orthorhombic structure; all members are antiferromagnetic [4–9].

$RMnO_3$ crystalize in orthorhombic structure when the size of R is larger than that of Dy, with antiferromagnetic order [10–14]. Otherwise, $RMnO_3$ crystalize in hexagonal structure, with 120-degree antiferromagnetic order [15].

$RFeO_3$ crystalize in orthorhombic structure; all members exhibit antiferromagnetism [15]. The hexagonal structures can be stabilized using thin film epitaxy or doping, resulting the 120-degree antiferromagnetic order [16–21] similar to that in h- $RMnO_3$. The plot includes the new data from this work.

$RNiO_3$, except for $LaNiO_3$ which crystalizes in rhombohedra structure with a paramagnetism, have orthorhombic structures with antiferromagnetism [22–24].

S2. K_3 lattice distortion in hexagonal $RFeO_3$ and $RMnO_3$

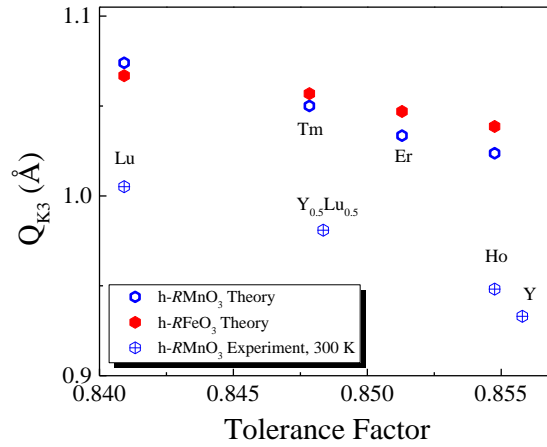


Figure S2. The K_3 lattice distortion in hexagonal $RFeO_3$ and $RMnO_3$.

In Fig. S2, we surveyed the K_3 lattice distortion of hexagonal $RFeO_3$ and $RMnO_3$. The experimental distortion amplitude (Q_{K_3}) was calculated from the crystal structure measured using neutron diffraction, since the oxygen positions are critical [25,26]. The theoretical distortion amplitudes calculated based on the first principles [27,28], are systematically larger than the experimental values but follow the similar trend.

S3. X-ray diffraction characterization of the h-ScFeO₃ films

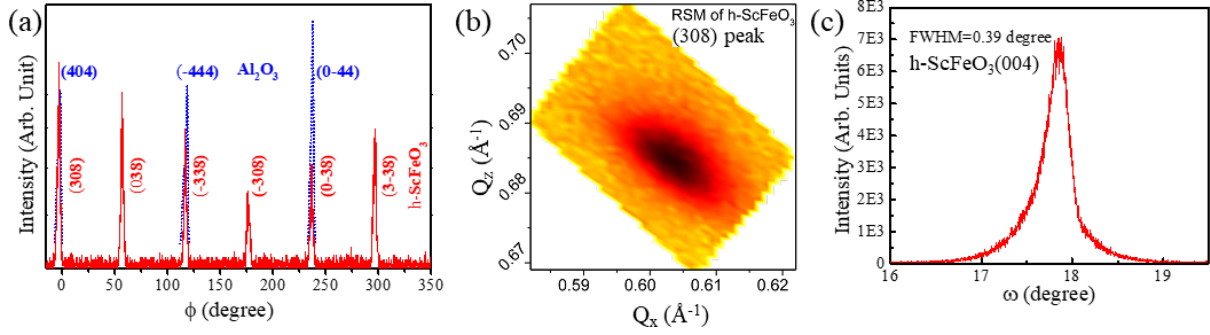


Figure S3. X-ray diffraction measurement on h-ScFeO₃(001)/Al₂O₃(001) films: (a) ϕ scan, (b) reciprocal space mapping (RSM) of the h-ScFeO₃ (308) peak, and (c) rocking curve on the h-ScFeO₃ (004) peak. The ϕ scan and RSM were measured on a Rigaku Smart Lab with 1.5406 Å x-ray wavelength while the rocking curve is measured using a Rigaku D/Max-B with 1.789 Å x-ray wavelength.

Figure S3 shows the x-ray diffraction characterization of h-ScFeO₃ films. Hexagonal coordinates are used for both the h-ScFeO₃ film and the Al₂O₃ substrate. As shown in Fig. S3(a), the three-fold and the six-fold rotational symmetries of Al₂O₃ and of h-ScFeO₃ respectively are revealed by the ϕ scan, consistent with their rhombohedral and hexagonal structures respectively. From the alignment of the peaks, the epitaxial relation in the basal plane h-ScFeO₃(100) || Al₂O₃(100) is revealed. In Fig. S3(b), the reciprocal space mapping around the h-ScFeO₃ (308) peak is plotted. From the peak position, one can calculate the lattice constants: $a = 5.742$ Å, and $c = 11.690$ Å. Figure S3(c) shows the rocking curve of the h-ScFeO₃ (004) peak. Using the Scherrer equation [30], one can estimate the in-plane size of the crystallites: $\frac{0.9\lambda}{\Delta\theta \cos\theta}$, where λ is the x-ray wavelength, $\Delta\theta$ is the full width half maximum (FWHM) in Fig. S3(c); the result shows the in-plane crystallite size is approximately 25 nm.

S4. Neutron diffraction measurements of the h-YbFeO₃ films

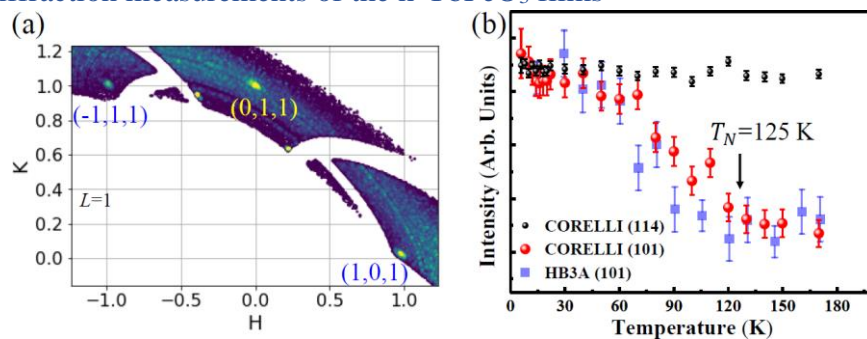


Figure S4. (a) A slice of the reciprocal space of h-YbFeO₃ at $L=1$ measured using neutron diffraction at CORELLI (see text). (b) Temperature dependence of the integrated neutron diffraction intensities of the (101) and (114) peaks measured at CORELLI and HB3A.

To study the magnetic ordering of h-YbFeO₃, we carried out neutron diffraction measurements. Figure S4(a) shows a slice of the reciprocal space at $L=1$. Three Bragg peaks (101), (011), and (-111), which are equivalent because of the six-fold rotational symmetry along the c axis, are observed. The (101) Bragg peak is forbidden for the nuclear diffraction due to the crystal structure symmetry of h-RFeO₃ (space group $P6_3cm$), but it is allowed for magnetic diffraction [29]. Figure S4(b) shows the temperature dependence of the integrated peak intensities for selected peaks. A clear change of the slope of the (101) peak intensity is observed at $125 \pm 5 \text{ K}$, suggesting a magnetic transition [Fig. S4(b)]. In contrast, the intensity of the (114) peak, which mainly comes from the nuclear scattering, shows an insignificant temperature dependence. The strong temperature dependence of the (101) peak is confirmed by single-crystal neutron diffraction at HB3A, as also shown in Fig. S4(b) and Fig. S5. The magnetic transition temperature of 125 K is consistent with the reported T_N for h-YbFeO₃ from magnetometry [20].

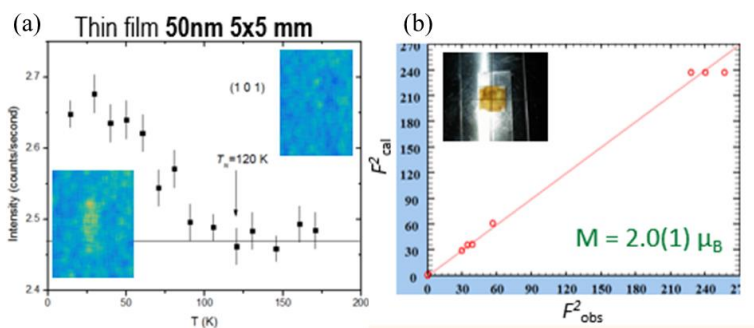


Figure S5. Neutron diffraction measurements on h-YbFeO₃ films at HB3A. (a) Diffraction intensity as a function of temperature for the (101) peak. The insets are the detector images showing the (101) peak at low temperature which vanishes at high temperature. (b) The calculated v.s. observed magnetic structural factors which lead to a magnetic moment of $2.0 \mu_B$ per Fe.

S5. Neutron diffraction data measured at the Spallation neutron source (SNS)

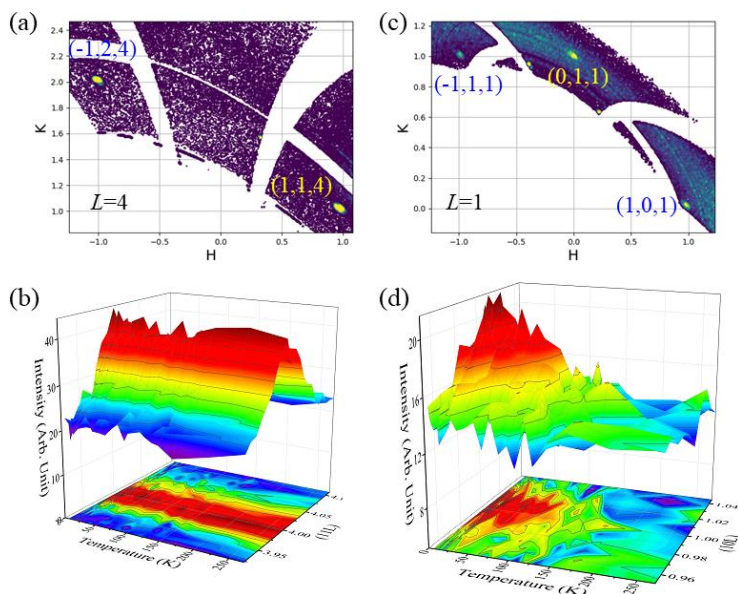


Figure S6. Neutron diffraction data of h-YbFeO₃. (a) and (c) are slices of three-dimensional reciprocal space at $L=4$ and $L=1$ respectively. (b) and (d) are the temperature dependence of the L scan near the Bragg diffraction points (1-24) and (011) respectively.

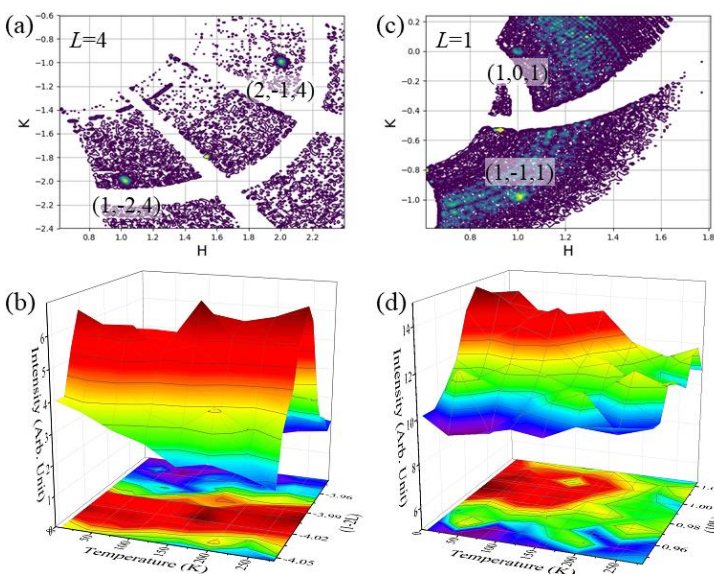


Figure S7. Neutron diffraction data of h-ScFeO₃. (a) and (c) are slice of three-dimensional reciprocal space at $L=4$ and $L=1$ respectively. (b) and (d) are the temperature dependence of the L scan near the Bragg diffraction points (1-24) and (101) respectively.

Elastic diffractions with unpolarized pulsed neutron beams were carried out on h-RFeO₃ films at the beamline CORELLI of the Spallation neutron source (SNS) with a pulsed neutron source. With the two-dimensional detector, and the pulsed neutron beam which contains neutrons with various wavelengths, a three-dimensional portion of the reciprocal space can be measured without rotating the sample. In this work, the incident angle of the neutron beam is set so that both the magnetic Bragg diffraction peak (101) and the nuclear Bragg diffraction peak (114) are included in this portion of the reciprocal space and measured at the same time.

Figure S6 and S7 show the raw data of the neutron diffraction on h-YbFeO₃ and h-ScFeO₃ respectively. Slices at $L=4$ and $L=1$ reveals the diffraction of (114) and (101) [Fig. S6 and S7 (a) and (b)] peaks and their equivalences respectively. The white space in the slices are parts of the

reciprocal space that are not covered by the detector. From the temperature dependence of the L scan, one can observe the disappearance of the magnetic diffractions peak (101) but not the nuclear diffraction peak (114) within the temperature range of the measurements. It is obvious that the transition temperature of h-ScFeO₃ is significantly higher than that of h-YbFeO₃.

S6. Dzyaloshinskii-Moriya (DM) interaction between Fe sites and the canting of the Fe spins in $h\text{-RFeO}_3$

- DM interactions

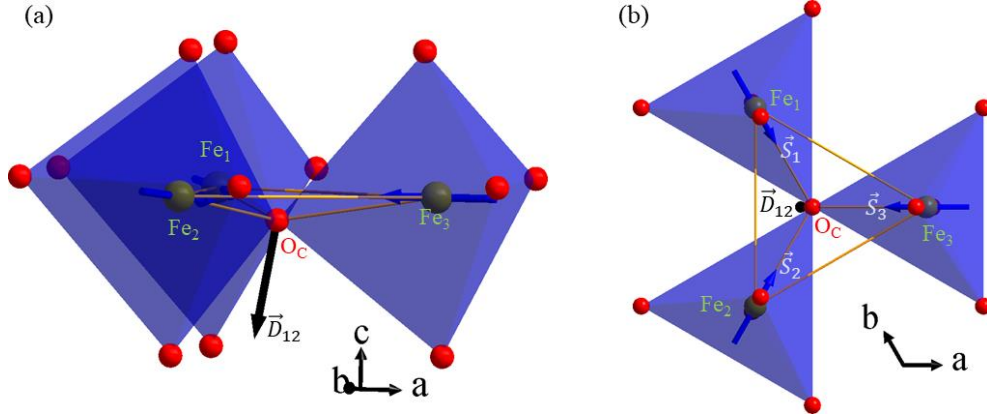


Figure S8. Schematics of the FeO₅ trimer. (a) Side view of the trimer highlighting the downward displacement of the atom O_C and the DM interaction vector between Fe₁ and Fe₂. (b) Top view of the trimer.

Here we discuss the DM interaction [31,32] using the symmetry analysis and the Keffer's estimation [33]. As shown in Fig. S8, the Fe sites in $h\text{-RFeO}_3$ trimerizes due to the collective tilt of the FeO₅. We can assume the positions of the three Fe atoms (Fe₁ to Fe₃) and the oxygen in the center (O_C) as

$$\begin{aligned}\vec{r}_{Fe1} &= \frac{a}{3} \left(-\frac{1}{2}, \frac{\sqrt{3}}{2}, 0 \right) \\ \vec{r}_{Fe2} &= \frac{a}{3} \left(-\frac{1}{2}, -\frac{\sqrt{3}}{2}, 0 \right) \\ \vec{r}_{Fe3} &= \frac{a}{3} (1, 0, 0) \\ \vec{r}_{O_C} &= (0, 0, -\delta),\end{aligned}$$

where a is the lattice constant in the basal plane of $h\text{-RFeO}_3$.

We analyze the DM interaction between Fe₁ and Fe₂ as an example. According to Moriya [31], the DM interaction between two magnetic ions results from the on-site spin-orbit coupling and the hopping between the electronic states of the magnetic ions through a diamagnetic atom (or atoms). The symmetry of the geometric arrangement of the two magnetic ions and the diamagnetic atom(s) is critical. For the DM interaction between Fe₁ and Fe₂, the symmetry of the Fe₁-O_C-Fe₂ connectivity determines the direction of the vector coefficient \vec{D}_{12} in the DM interaction $\vec{D}_{12} \cdot (\vec{S}_1 \times \vec{S}_2)$. Two symmetry rules [31] can be applied here: 1) if there is a mirror plane including Fe₁ and Fe₂, $\vec{D}_{12} \perp$ the mirror plane; 2) if there is a mirror plane perpendicular to $\vec{r}_{Fe1} - \vec{r}_{Fe2}$ that passes the point $\frac{\vec{r}_{Fe1} + \vec{r}_{Fe2}}{2}$, $\vec{D}_{12} \parallel$ the mirror plane. Therefore, \vec{D}_{12} is perpendicular to the plane including the Fe₁-O_C-Fe₂ atoms.

According to Keffer [33], if the DM interaction is mediated mainly by one diamagnetic atom, one can estimate the magnitude and the orientation of the vector interaction coefficient as $\vec{D}_{i,j} \propto \vec{r}_{i3} \times \vec{r}_{j3}$, where \vec{r}_{i3} and \vec{r}_{j3} are the vectors from the two magnetic ions to the diamagnetic (3rd) atom respectively. In the case of Fe₁-O_C-Fe₂,

$$\vec{D}_{12} \propto \vec{r}_{Fe1O_C} \times \vec{r}_{Fe2O_C} = \left(\frac{a\delta}{\sqrt{3}}, 0, \frac{\sqrt{3}a^2}{18} \right),$$

where $\vec{r}_{Fe1O_C} = \vec{r}_{Fe1} - \vec{r}_{O_C}$ and $\vec{r}_{Fe2O_C} = \vec{r}_{Fe2} - \vec{r}_{O_C}$.

Assuming $\vec{D}_{12} = -D(\sin \phi, 0, \cos \phi)$, one finds

$$\tan \phi = \frac{6\delta}{a}.$$

Note that the tilt angle of the FeO₅ local environment can be defined using $\tan \gamma = \frac{\delta}{a/3} = \frac{3\delta}{a}$. Since all the angles are small (in h-LuFeO₃, $\gamma \approx 9.5$ degree), one finds approximately

$$\gamma \approx \frac{3\delta}{a}, \phi \approx \frac{6\delta}{a}.$$

In addition, since $\delta \ll a$, the magnitude of DM interaction strength follows

$$D \propto a^2.$$

- **Canting of the Fe spin and the DM interaction**

The canting of Fe spins mainly comes from the DM interaction and the tilt of the FeO₅ local environment which tilts the vector coefficient $\vec{D}_{i,j}$ (by angle ϕ) and causes the Fe spins to reorient to minimize the DM interaction energy $\vec{D}_{i,j} \cdot (\vec{S}_i \times \vec{S}_j)$. At the same time, canting of the Fe spins reduces the Fe-Fe spin angle and increases the antiferromagnetic exchange interaction. Therefore, the canting angle θ is a result of the competition between the exchange interaction and the DM interaction. Below, we derive the relation between θ and ϕ (the tilt angle of $\vec{D}_{i,j}$).

As shown in Fig. S8 we can assume the spin vectors as the following

$$\vec{S}_1 = \left(\frac{1}{2} \cos \theta, -\frac{\sqrt{3}}{2} \cos \theta, -\sin \theta \right) S$$

$$\vec{S}_2 = \left(\frac{1}{2} \cos \theta, \frac{\sqrt{3}}{2} \cos \theta, -\sin \theta \right) S$$

$$\vec{S}_3 = (-\cos \theta, 0, -\sin \theta) S,$$

where S the magnitude of the Fe spin.

We consider the exchange interaction between the spins \vec{S}_1 and \vec{S}_2 as an example, which shows

$$E_{12}^{(ex)} = J \vec{S}_1 \cdot \vec{S}_2 = J \left(-\frac{1}{2} + \frac{3}{2} \sin^2 \theta \right) S^2,$$

where $J > 0$ is the exchange interaction coefficient.

For the DM interaction, if we assume $\vec{D}_{12} = -D(\sin \phi, 0, \cos \phi)$, where $D > 0$ is the magnitude of the interaction (see above discussion), the interaction energy is

$$E_{12}^{(DM)} = \vec{D}_{12} \cdot (\vec{S}_1 \times \vec{S}_2) = -D(\sqrt{3} \sin \theta \cos \theta \sin \phi + \frac{\sqrt{3}}{2} \cos^2 \theta \cos \phi).$$

The canting angle θ will be determined by the minimization of the total energy $E_{12}^{(ex)} + E_{12}^{(DM)}$. By noting that both θ and ϕ are small, one can make the approximation that

$$E_{12}^{(ex)} + E_{12}^{(DM)} \approx J \left(-\frac{1}{2} + \frac{3}{2} \theta^2 \right) - D \left(\sqrt{3} \theta \phi + \frac{\sqrt{3}}{2} \right).$$

Therefore, the minimization results in

$$\theta \approx \frac{D}{\sqrt{3}J} \phi.$$

Since it is expected that the DM interaction is much weaker than the exchange interaction (or $D \ll J$), one expects $\theta \ll \phi$, which agrees with the experimental observation (typically ϕ is a few degrees while θ is a fraction of a degree).

According to the discussion above, $D \propto a^2$, where a is the lattice constant of the basal plane. Hence the canting angle of the Fe spin follows

$$\theta \propto \frac{2a^2\phi}{\sqrt{3}J} = \frac{4a^2\gamma}{\sqrt{3}J}.$$

In the case of hexagonal ferrites, the smaller R leads to larger ϕ , which decreases J , but also decreases a . Thus, it is possible that the combined effect may lead to a reduction of the canting angle θ under the compressive strain.

- [1] A. S. Bhalla, R. Guo, and R. Roy, *Mater. Res. Innov.* **4**, 3 (2000).
- [2] R. D. Shannon, *Acta Cryst.* **A32**, 751 (1976).
- [3] H. D. Zhou and J. B. Goodenough, *J. Phys. Condens. Matter* **17**, 7395 (2005).
- [4] E. F. Bertaut, G. Bassi, G. Buisson, P. Burlet, J. Chappert, A. Delapalme, J. Mareschal, G. Roullet, R. Aleonard, R. Pauthenet, and J. P. Rebouillat, *J. Appl. Phys.* **37**, 1038 (1966).
- [5] T. Sakai, G. Y. Adachi, J. Shiokawa, and T. Shin-Ike, *J. Appl. Phys.* **48**, 379 (1977).
- [6] A. Muñoz, A. Alonso, T. Casáis, J. Martínez-Lope, L. Martínez, and T. Fernández-Díaz, *Phys. Rev. B - Condens. Matter Mater. Phys.* **68**, 1 (2003).
- [7] M. Reehuis, C. Ulrich, P. Pattison, B. Ouladdiaf, M. C. Rheinstädter, M. Ohl, L. P. Regnault, M. Miyasaka, Y. Tokura, and B. Keimer, *Phys. Rev. B - Condens. Matter Mater. Phys.* **73**, 1 (2006).
- [8] M. Reehuis, C. Ulrich, K. Proke, S. Mat’A, J. Fujioka, S. Miyasaka, Y. Tokura, and B. Keimer, *Phys. Rev. B - Condens. Matter Mater. Phys.* **83**, 1 (2011).
- [9] C. Ritter, S. A. Ivanov, G. V. Bazuev, and F. Fauth, *Phys. Rev. B* **93**, 1 (2016).
- [10] F. Moussa, M. Hennion, J. Rodriguez-Carvajal, H. Moudden, L. Pinsard, and A. Revcolevschi, *Phys. Rev. B* **54**, 15149 (1996).
- [11] Z. Jiráček, J. Hejtmánek, E. Pollert, M. Maryško, M. Dlouhá, and S. Vratislav, *J. Appl. Phys.* **81**, 5790 (1997).
- [12] A. Muñoz, J. A. Alonso, M. J. Martínez-Lope, J. L. García-Muñoz, and M. T. Fernández-Díaz, *J. Phys. Condens. Matter* **12**, 1361 (2000).
- [13] J. G. Cheng, J. S. Zhou, J. B. Goodenough, Y. T. Su, Y. Sui, and Y. Ren, *Phys. Rev. B* **84**, 1 (2011).
- [14] T. Kimura, G. Lawes, T. Goto, Y. Tokura, and A. P. Ramirez, *Phys. Rev. B* **71**, 224425 (2005).
- [15] M. Fiebig, T. Lottermoser, and R. V. Pisarev, *J. Appl. Phys.* **93**, 8194 (2003).
- [16] S. M. Disseler, J. A. Borchers, C. M. Brooks, J. A. Mundy, J. A. Moyer, D. A. Hillsberry, E. L. Thies, D. A. Tenne, J. Heron, M. E. Holtz, J. D. Clarkson, G. M. Stiehl, P. Schiffer, D. A. Muller, D. G. Schlom, and W. D. Ratcliff, *Phys. Rev. Lett.* **114**, 217602 (2015).
- [17] H. Yokota, T. Nozue, S. Nakamura, H. Hojo, M. Fukunaga, P. E. Janolin, J. M. Kiat, and A. Fuwa, *Phys. Rev. B* **92**, 054101 (2015).
- [18] S.-J. Ahn, J.-H. Lee, H. M. Jang, and Y. K. Jeong, *J. Mater. Chem. C* **2**, 4521 (2014).
- [19] J. A. Moyer, R. Misra, J. A. Mundy, C. M. Brooks, J. T. Heron, D. A. Muller, D. G. Schlom, and P. Schiffer, *APL Mater.* **2**, 012106 (2014).
- [20] Y. K. Jeong, J. Lee, S. Ahn, S.-W. Song, H. M. Jang, H. Choi, and J. F. Scott, *J. Am. Chem. Soc.* **134**, 1450 (2012).
- [21] S. M. Disseler, X. Luo, B. Gao, Y. S. Oh, R. Hu, Y. Wang, D. Quintana, A. Zhang, Q. Huang, J. Lau, R. Paul, J. W. Lynn, S. W. Cheong, and W. Ratcliff, *Phys. Rev. B* **92**, 054435 (2015).

- [22] M. L. Medarde, *J. Phys. Condens. Matter* **9**, 1679 (1997).
- [23] J. A. Alonso, M. J. Martínez-Lope, M. T. Casais, J. L. Martínez, G. Demazeau, A. Largeteau, J. L. García-Muñoz, A. Muñoz, and M. T. Fernández-Díaz, *Chem. Mater.* **11**, 2463 (1999).
- [24] M. T. Fernández-Díaz, J. A. Alonso, M. J. Martínez-Lope, M. T. Casais, and J. L. García-Muñoz, *Phys. Rev. B* **64**, 1444171 (2001).
- [25] A. Munoz, J. Alonso, M. Martinez-Lopez, M. Cesais, J. Martinez, and M. Fernandez-Diaz, *Chem. ...* **13**, 1497 (2001).
- [26] S. Lee, A. Pirogov, M. Kang, K. H. Jang, M. Yonemura, T. Kamiyama, S. W. Cheong, F. Gozzo, N. Shin, H. Kimura, Y. Noda, and J. G. Park, *Nature* **451**, 805 (2008).
- [27] H. Tan, C. Xu, M. Li, S. Wang, B. L. Gu, and W. Duan, *J. Phys. Condens. Matter* **28**, 126002 (2016).
- [28] C. Xu, Y. Yang, S. Wang, W. Duan, B. Gu, and L. Bellaiche, *Phys. Rev. B* **89**, 205122 (2014).
- [29] A. Munoz, J. A. Alonso, M. J. Martinez-Lope, M. T. Casais, J. L. Martinez, and M. T. Fernandez-Diaz, *Phys. Rev. B* **62**, 9498 (2000).
- [30] B. D. Cullity, *Elements of X-Ray Diffraction*. (Addison-Wesley Pub. Co., Reading, Mass., 1956).
- [31] T. Moriya, *Phys. Rev.* **120**, 91 (1960).
- [32] I. Dzyaloshinsky, *J. Phys. Chem. Solids* **4**, 241 (1958).
- [33] F. Keffer, *Phys. Rev.* **126**, 896 (1962).